

Article

A low-cost instrument for multidimensional characterization of advanced wireless communication technologies

Rodrigo Gounella¹, Augusto Martins², Vinicius Pepino¹, Ben-Hur Borges¹ and João Paulo Carmo^{1*}

¹ Metamaterials Group: Microwaves and Optics (GMeta), Dept. of Electrical and Computer Engineering (SEL), University of São Paulo (USP), Avenida Trabalhador São-Carlense, Nr. 400, Parque Industrial Arnold Schimidt, CEP 13566-590, São Carlos – SP, Brazil; rodrigogounella@usp.br (R.H.), vinicius.pepino@usp.br (V.P.), ben-hur@sc.usp.br (B.-H.V.B), and jcarmo@sc.usp.br (J.P.C.)

² Department of Physics and Astronomy, University of Manchester, Oxford Road, Manchester, M13 9PL, United Kingdom; augusto.martinezalves@manchester.ac.uk (A.M.)

* Correspondence: jcarmo@sc.usp.br

Abstract: 3D printing is commonly used to create complex objects at a low cost. It has also been applied in the fabrication of metamaterials and metasurfaces, which alter the propagation path of electromagnetic waves. These structures have diverse applications, including enhancing beam direction, improving antenna gain and signal-to-noise ratio, and creating filters and reflectors. Metasurfaces are cheap to fabricate and their use is expected to boost antenna efficiency in 5G telecommunications and beyond. However, accurately characterizing their profile remains a significant challenge. This paper presents a low-cost fully automated 4-axis instrument for microwave metasurface characterization, overcoming limitations of manual methods and offering an efficient and accurate approach. This research represents a significant advancement in microwave metasurface characterization, enabling sophisticated techniques to advance wireless communication technologies, as it is the case of the future 5G and millimeter-wave communication systems. The equipment has an approximate cost of \$1550 USD and was able to characterize a metalens with a focal distance of 20 cm designed for signals at 30 GHz. It was possible to create 2D and 3D profiles of the intensity distribution focused by the metalens and extract parameters such as the gain (8.05 dB), 3dB depth of focus (11 cm) and full width at half maximum (2.17 cm). The comparison of the measurements with the diffraction calculations of the metalens showed a very good agreement between the intensity distributions and the parameters of the metalens.

Keywords: low-cost instrumentation, characterization setup, multidimensional characterization, metasurfaces, millimeter-wave.

1. Introduction

Additive manufacturing technologies, such as 3D printing, have been widely used in the fabrication of complex objects at low cost. Recently, the application of these technologies has been extended to the fabrication of metamaterials and metasurfaces, which are capable to modify the propagation of electromagnetic waves. These structures can be used to improve beam directivity, generate Gaussian and Bessel beams, increase antenna gain, and improve signal-to-noise ratio [1–7].

Metasurfaces are artificial structures that are designed to module the propagation of electromagnetic waves at various frequencies. They are composed of a series of subwavelength elements that can be 3D printed by metal or thermoplastic, milled and cutted [8,9], making their fabrication relatively simple and inexpensive. Metasurfaces have numerous applications, such as flat-focusing lenses [7,10], frequency-selective filters [11], reflectors [12], polarizers [13], and broadband absorbers [14].

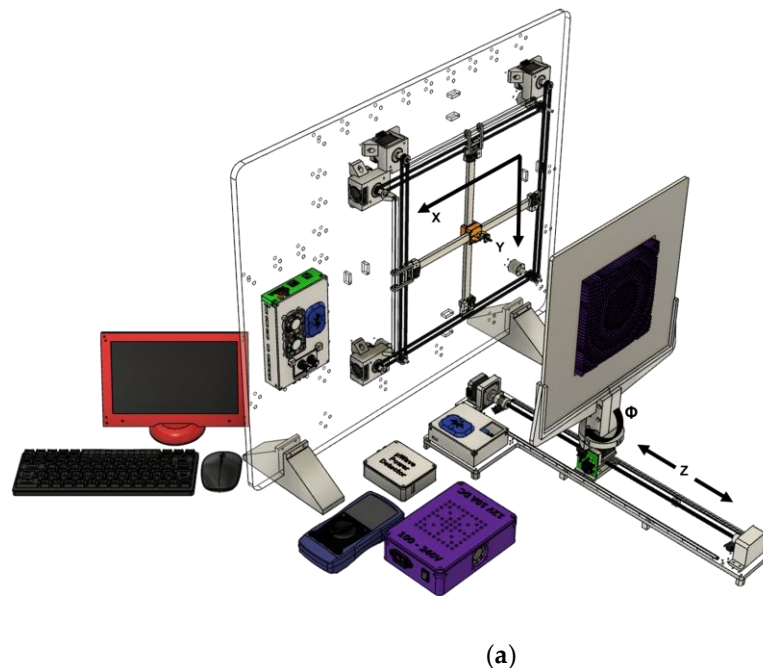
One of the most promising applications of metasurfaces is in the field of telecommunications, specifically in 5G. With the increasing demand for higher data rates and wider network coverage, metasurfaces have the potential to significantly improve antenna efficiency and therefore signal quality [15–17]. However, characterizing the profile generated by these structures is a significant challenge.

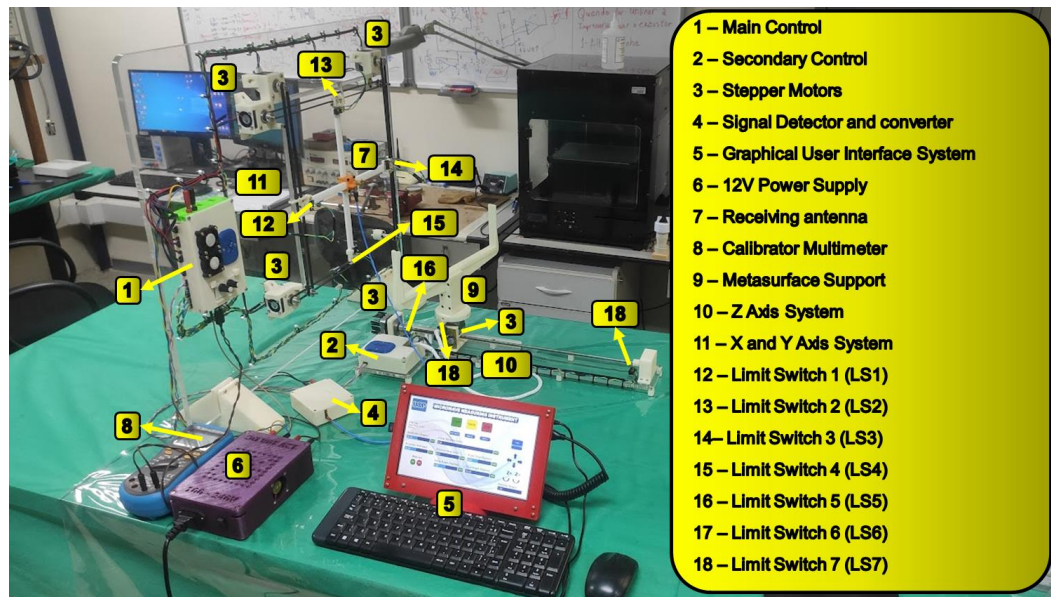
In this context, this paper presents a low-cost instrument for multidimensional characterization of advanced wireless communication devices, which is fully automated with 4-axis and capable of collecting more than 1.6 million measures of X-Y axis sweeping, translating in Z axis with approximately 5 μm of precision and rotating 360° with 1.8° of resolution for fully image reconstruction and structure characterization. This paper also validates the suitability of this low-cost instrument, by characterizing and verifying with simulation results, a known component, e.g., a previously fabricated metasurface. It must be noted that surprisingly, neither automated instruments for microwave characterization nor metasurface characterization and image reconstruction are currently available in the literature. Usually, such experiments use a somewhat archaic and manual setup, making the device characterization process not only tiresome, but also error prone.

This paper is organized as follows: Section 2 presents the system overview with its main components; Section 3 presents details of instrument hardware; Section 4 presents the hardware integration; Section 5 presents a Graphical User Interface developed to control the instrument and the performance in terms of time, accuracy and resolution; Section 6 presents an application of the instrument characterizing a 30GHz metalens bringing the results and discussion and Section 7 presents the conclusions.

2. System overview

All components of our instrument were primarily designed and constructed using 3D CAD software, specifically Autodesk Fusion 360 Academic License. These components were then fabricated using a GLC-1490 laser cutter from Glorystar Laser Technology Company and a GTMax 3D Core A1 3D printer, using acrylic and ABS materials, respectively. The instrument parts were assembled with different sizes M3 screws and nuts. Figure 1(a) depicts the 3D design of the instrument, while Figure 1(b) displays a photograph of the fully assembled instrument.





(b)

Figure 1. (a) The three-dimensional design of the instrument made in Autodesk Fusion 360 Academic License. (b) A photograph of assembled instrument and its components.

It was used a Vector Network Analyzer (VNA) Rohde & Schwarz (R&D) ZVA-40 worked as a signal generator and produce a signal with a power of +15 dBm and a frequency of 30GHz. This equipment has the capability to produce signals within the frequency range of 10MHz to 40GHz. The signal power varies based on frequency, with the typical signal power range for frequencies of 20GHz to 32GHz being -40dBm to +15dBm [18]. The signal was transmitted using a WR-34 horn antenna from Pasternack, which has a nominal gain of 20dBi and a 17° (17.4°) vertical (horizontal) half-power beamwidth (HPBW) [19]. A schematic representation of the system overview utilized to characterize metasurfaces using the instrument described in Figure 1 is shown in Figure 2.

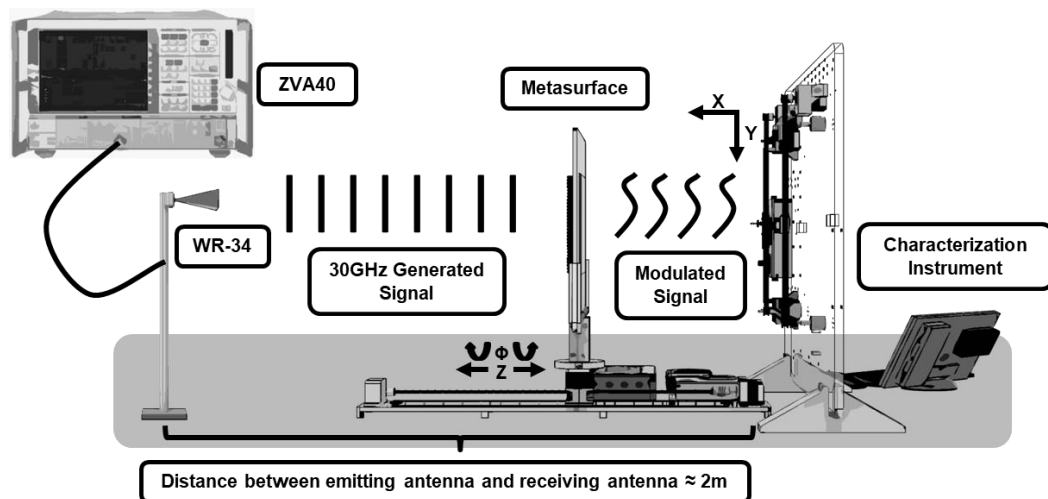


Figure 2. Entire System Overview with the representation of all main components. The VNA ZVA40 working as a 30GHz signal generator connected with the WR-34 horn antenna emitting the signal. The signal generated and emitted passes through the metasurface interacting with the manufactured structures and reaching the helical antenna installed in the instrument. The received signal is then processed and the intensity in XYZ is stored for later analysis.

After being transmitted by the metasurface, the signal is received by a helical antenna [20]. This type of antenna was selected to compose the prototype due to its ease of design and fabrication and

it has reduced dimensions, which allow for a higher spatial resolution. Figure 3 presents the design specifications for the helical antenna used in this research.

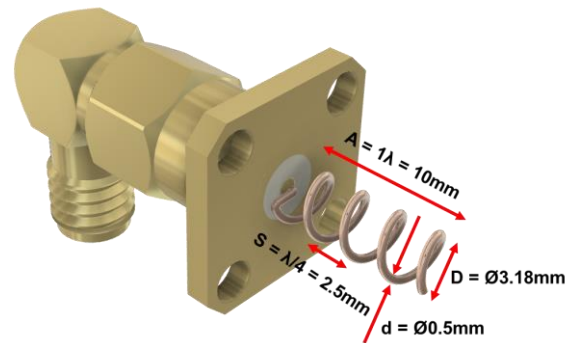


Figure 3. Helical Antenna Design. The helical antenna was fabricated with a copper wire and it was welded in a SMA connector base. This antenna has been designed to operate at a frequency of 30GHz. It consists of four turns, measuring one wavelength in length, with a spacing between the turns of one-quarter wavelength. The diameter of the helices measures 3.18mm.

The fabricated antenna was designed to have low return loss at 30GHz with a length equal to the operating wavelength (10mm), an inter-helix spacing (S) equals to $\lambda/4$ and a diameter (D) of 3.18mm, as shown in Figure 3. A photo of the antenna can be seen in the inset of Figure 4(a). Figure 4(a) shows the measured return loss of the antenna as function of the operating frequency obtained with the VNA. Note that the return loss minimum was actually at a slightly higher frequency of 30.88GHz, as shown by Figure 4(b). This is probably due to small deviations on the fabricated antenna length.

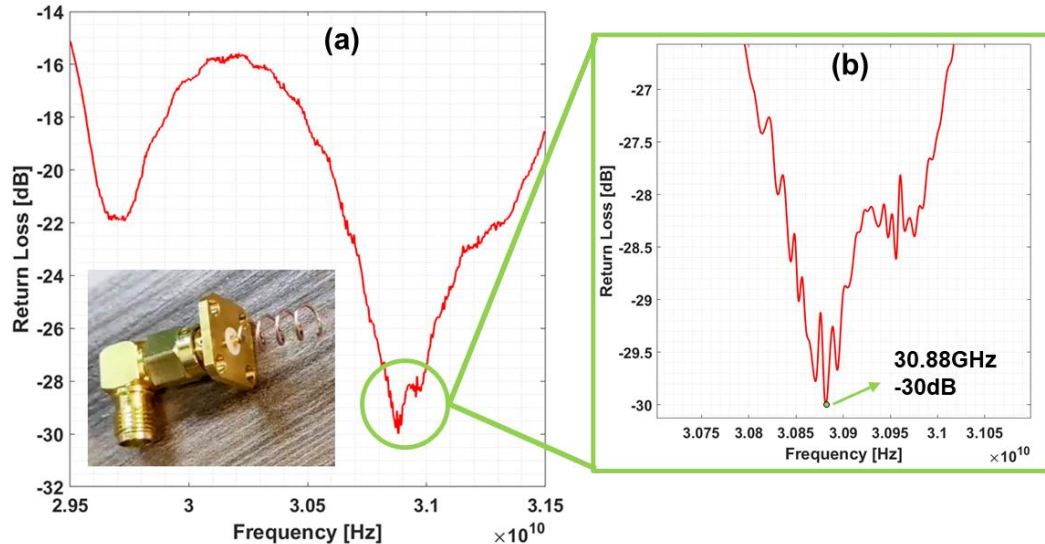


Figure 4. (a) and (b) show the measured return loss of the fabricated helical antenna (a photo can be seen in inset of (a)) at different frequency ranges. The measurement was done with the VNA.

3. Hardware

Figure 5 displays the hardware schematic of our assembled instrument, which consists of three Printed Circuit Boards (PCBs) designed using Fusion 360 electronics design software. The PCBs were fabricated using the ProtoMat S103 PCB milling machine from LPKF Laser & Electronics.

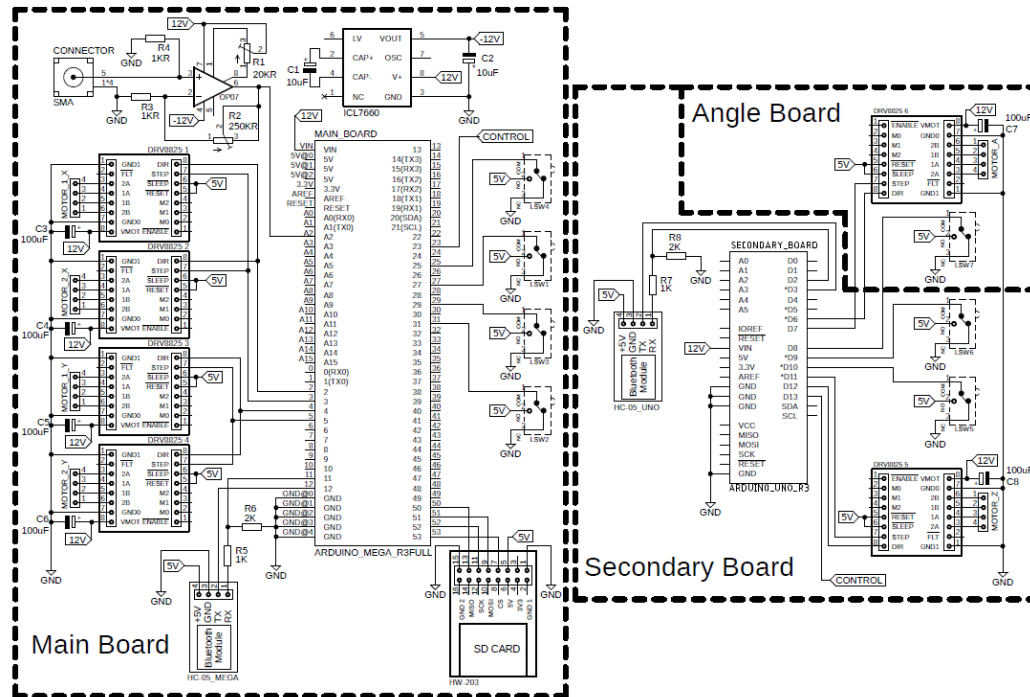


Figure 5. Instrument Hardware schematic.

The main board is equipped with an Arduino Mega 2560, which serves as the primary controller for the instrument. The Arduino Mega 2560 is a microcontroller-based board which has 54 digital input/output pins, 15 of which can be used as PWM outputs, 16 analog inputs, 4 UARTs (hardware serial ports), a 16MHz crystal oscillator, a USB connection, a power connector, an ICSP connector, and a reset button. The microcontroller features 256KB of Flash memory, 8KB of which is occupied by the board's bootloader, 8KB of SRAM memory, and 4KB of EEPROM memory.

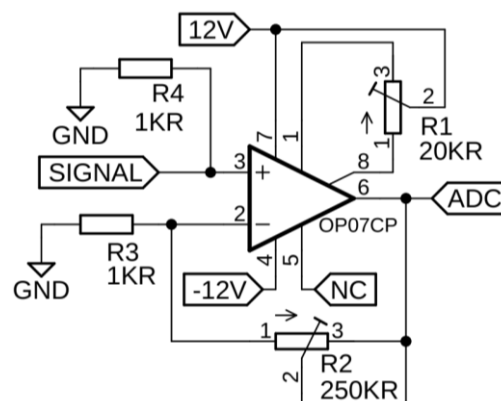
The secondary board features an Arduino Uno, which is responsible for controlling the Z-axis translation and angle board rotation of the characterized metasurface in the instrument. The Arduino Uno is a microcontroller-based board with 14 digital input/output pins, 6 of which can be used as PWM outputs, 6 analog inputs, a 16MHz ceramic resonator, a USB connection, a power connector, an ICSP connector, and a reset button. The microcontroller has 32KB of Flash memory, 0.5KB of which is occupied by the board's bootloader, 2KB of SRAM memory, and 1KB of EEPROM memory.

The receiver antenna can move on the XY plane whereas the metasurface can move on the Z direction and rotate along the Z axis as can be seen in Figure 1(a). Each of these degrees of freedom is actuated by a Nema 17 HS4401 stepper motor that is driven by a DRV8825 driver. The translation is aided by a threaded shaft. Each stepper motor has a torque of 0.42N.m, uses up to 1.7A per phase, and has a resolution of 1.8° per step with 200 steps per turn. The motors measure 42x42x40mm and weigh 280g. The DRV8825 features an adjustable SMD potentiometer for current limiting, overcurrent and overtemperature protection, and the ability to operate with up to six microstep resolutions (1, 1/2, 1/4, 1/8, 1/16, and 1/32 step). It operates from 8.2V to 45V and can deliver up to approximately 1.5A per phase without a heat sink or forced airflow. With proper heat dissipation, this driver can reach up to 2.2A per coil.

The data collected is stored on a SD card using an SD card module HW-203 installed on the main board. The received RF signal is directed to a LTC5596 RMS power detector from Analog Devices, which is mounted on a DC2158A evaluation board. The LTC5596 is a high-precision power detector that offers a wide RF input bandwidth from 100 MHz to 40 GHz, with a linear response in dB and a logarithmic slope of 29mV/dB over a dynamic range of 35dB with accuracy typically better than ± 1 dB. Figure 6 illustrates the instrument's signal conversion system, which includes a 3D printed case to shelter the components, connectors and a power switch (a), a DC2158A evaluation

Figure 1 consists of three photographs labeled (a), (b), and (c).
 (a) shows the top of a white 3D printed case with the text "uWave Power Detector" embossed on it.
 (b) shows the bottom of the same case, revealing the internal electronic components. A red box highlights the "DC2158A Board" and another red box highlights the "Voltage Regulator".
 (c) is a close-up of the circuit board, showing the "LTC5596 IC" and two ports labeled "RF IN" and "DC OUT".

Following the DC conversion, the signal is directed to an operational amplifier (OP07) integrated within the main board of the instrument. The OP07 operates with very low input offset voltage of $75\mu\text{V}$ achieved by trimming of the wafer stage, which eliminates the requirement for suppression by external components in most cases. Additionally, the OP07 features low input bias current of $\pm 4\text{nA}$ and high open-loop gain of 200V/mV . This combination of high open-loop gain, and low offset voltage make the OP07 particularly useful for high-gain instrumentation applications. The amplifier was installed in a non-inverting configuration, as the power detector delivers a positive DC voltage. The OP07 negative feedback is provided by an ICL7660 which converts the supply voltage from positive to negative over an input range of 1.5V to 12V , resulting in complementary output voltages from -1.5V to -12V . Our instrument has been designed to accommodate a wide range of applications; thus the amplifier gain is configurable. Figure 7 illustrates that the amplifier gain can be modified according to the operator's needs through the use of a $250\text{K}\Omega$ potentiometer (R2) and a $1\text{K}\Omega$ precision resistor (R3). Furthermore, R1, another potentiometer, is utilized for offset nulling, as described in [21].



The instrument's main and secondary controls communicate with a graphical user interface (GUI) developed on a Raspberry Pi 4 to receive initial measurement parameters, pause the measurement, or reset the microcontrollers to restart. This communication is facilitated through Bluetooth using two HC-05 Bluetooth modules installed on the main control and secondary control shields.

The HC-05 is a class 2 Bluetooth module with a serial port profile, capable of being configured as either a master or slave. The Bluetooth communication protocol used is v2.0+EDR with a 2.4GHz frequency in the ISM band and GFSK modulation.

4. Hardware integration

The microcontroller on the instrument main board controls the movement of the stepper motors by sending direction and step signals to four DRV8825 drivers, which are also installed on the main board. These signals then drive the four Nema 17 motors, enabling movement on the X (horizontal) and Y (vertical) axes. Two motors are controlled by a step and direction signal for movement on the X axis, and the other two motors are controlled by a separate step and direction signal for movement on the Y axis, all while adhering to the parameters received via Bluetooth from the GUI running on a Raspberry Pi 4.

Data acquisition is primarily performed by the receiving antenna, which directs the signal through a Thorlabs RF cable model KMM36 to the LTC5596 power detector board. This board converts the RF signal into a DC signal, which is then sent to the OP07 operational amplifier on the main board's shield. The analog input of the Arduino Mega microcontroller reads the DC signal and stores it on an SD card in a matrix form. The antenna begins the measurement in the upper right corner of the instrument and moves from right to left, collecting data as configured in the GUI. After reaching the end of the course, it moves down and back from left to right, collecting more data until reaching the bottom of the instrument. Finally, the antenna returns to the starting point in the upper left corner.

Upon completion of the matrix data collection, the Arduino Mega sends a control signal to the Arduino Uno on the secondary shield, which controls two Nema 17 motors to perform the Z axis translation and rotation movement of the metasurface being characterized. After the Z axis translation movement or rotation is complete, the Arduino Uno sends a control signal back to the Arduino Mega, and the process repeats. Figure 8(a) shows front of the main board cover case with the fans to cool down the motor drivers and the potentiometers to adjust the operational amplifier offset and gain, (b) shows the back of main board cover case with HC-05 bluetooth module fixed, (c) shows the main board with mounted Arduino Mega 2560, X and Y axis DRV8825 motor drivers, ICL7660 voltage converter, OP07 operational amplifier and the HW-203 SD Card Module, (d) shows the front of secondary board cover case with 3D printed Bluetooth Symbol that fix the HC-05 Bluetooth Module in the back of cover case (same for main board case), (e) shows the secondary board with mounted Arduino Uno and Z axis DRV8825 motor driver, (f) shows the back of secondary cover case with HC-05 bluetooth module fixed, (g) shows the angle board with DRV8825 motor driver responsible for supply and control metasurface rotation stepper motor.

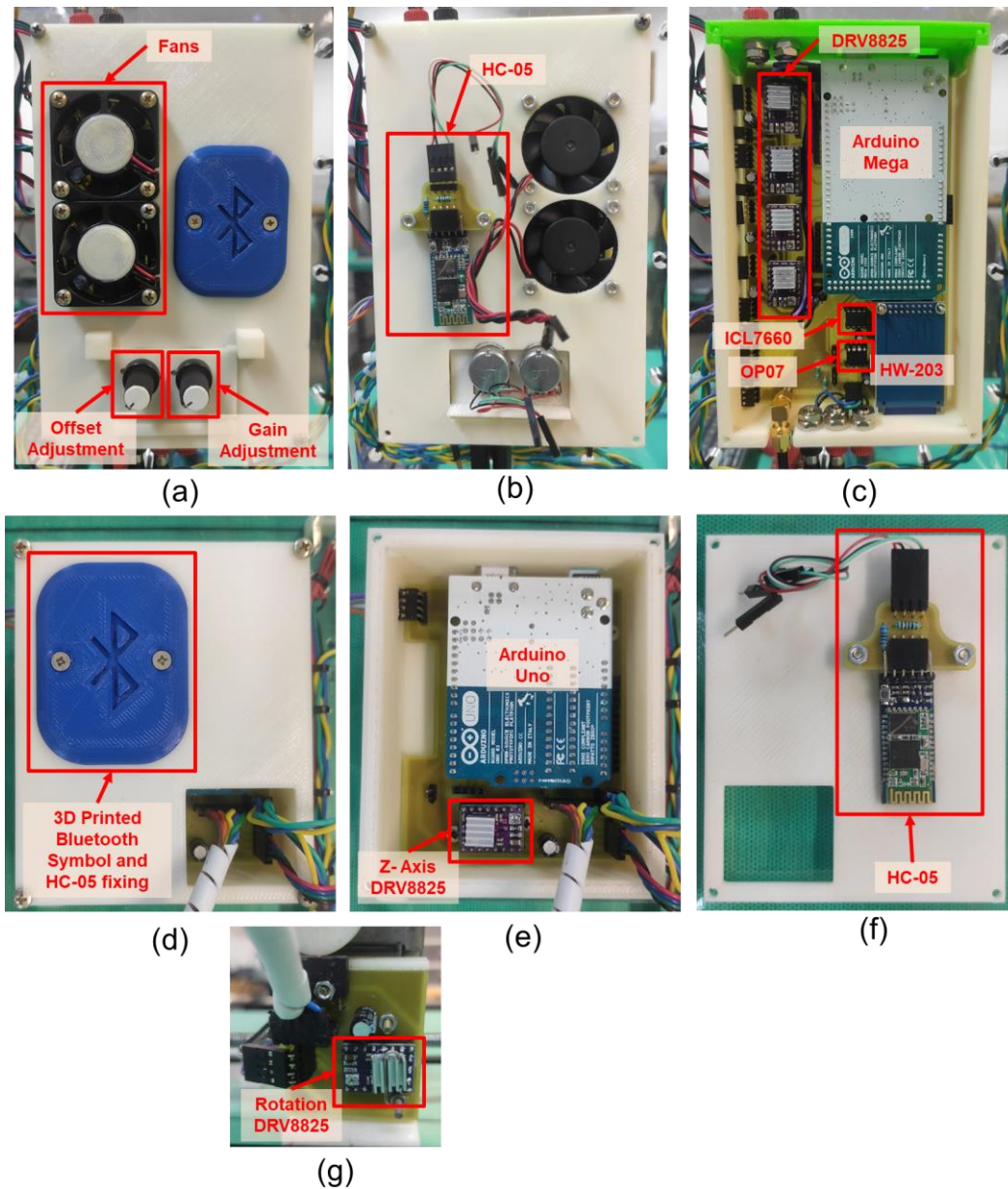


Figure 8. Photograph of instrument hardware integration. (a) Front of the main board cover case. (b) Back of main board cover case. (c) Main board. (d) Front of secondary board cover case. (e) Secondary board. (f) Back of secondary cover case. (g) Angle board.

5. Graphical User Interface (GUI)

The Processing Development Environment is an open-source programming language and Integrated Development Environment (IDE). This IDE was used in the development of an instrument Graphical User Interface (GUI). Figure 9 depicts the GUI screen running on the Raspberry Pi 4.

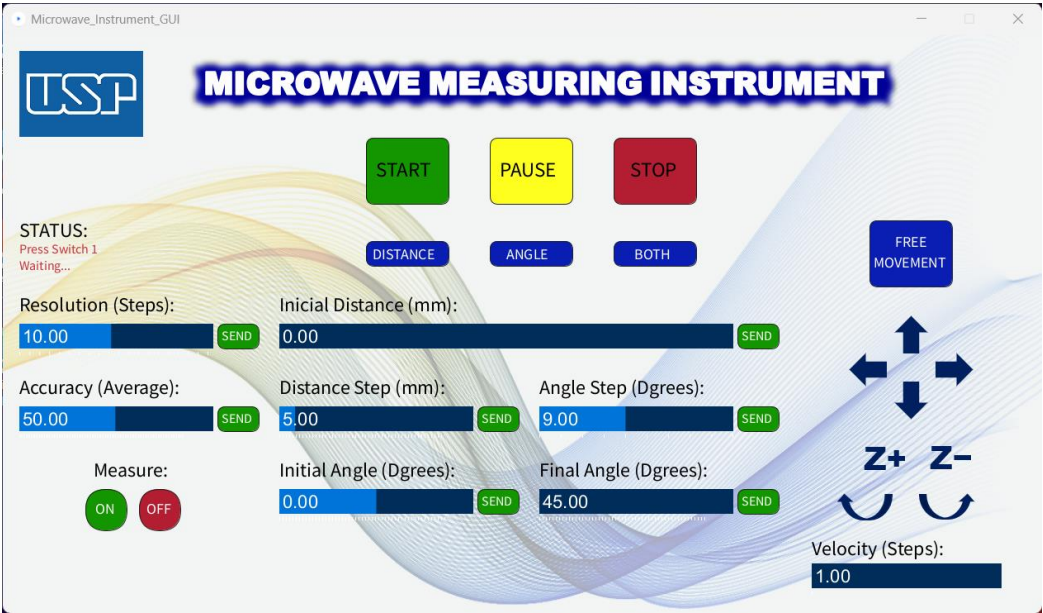


Figure 9. Developed Instrument GUI running in the Raspberry Pi 4.

At the top of the GUI, there are three buttons, START, PAUSE and STOP, as depicted in Figure 9. The START button has multiple functions, primarily to activate the instrument. This button is used to trigger the start signal to the Arduino Mega Microcontroller, to advance the OP07 operational amplifier gain configuration, and to resume measurements if the PAUSE button has been pressed. The PAUSE button is used to pause the motors and measurement collection, and the instrument remains paused until either the START or STOP button is pressed. The STOP button resets the microcontrollers, sending a reset command and restarting the entire characterization process.

The sequence of actions to be taken on the GUI to configure the instrument parameters is displayed to the operator as a text message in the "STATUS:" field located below and to the left of the START, PAUSE, and STOP buttons, as shown in Figure 9.

After configuring the operational amplifier gain and offset, it is necessary to define the resolution of the matrix data to be collected. This is done through the RESOLUTION slider, which sets the number of steps that the motors will rotate in each measurement. The operator sets the slider position and then clicks the SEND button next to the slider. A smaller number of steps results in a higher resolution matrix, with the time to complete a measurement being inversely proportional to the square of the resolution. The highest configurable resolution is 1 step, which corresponds to a matrix with 1200x1200 pixels, and the lowest resolution is 20 steps, which corresponds to a matrix with 60x60 pixels, as shown in Figure 10.

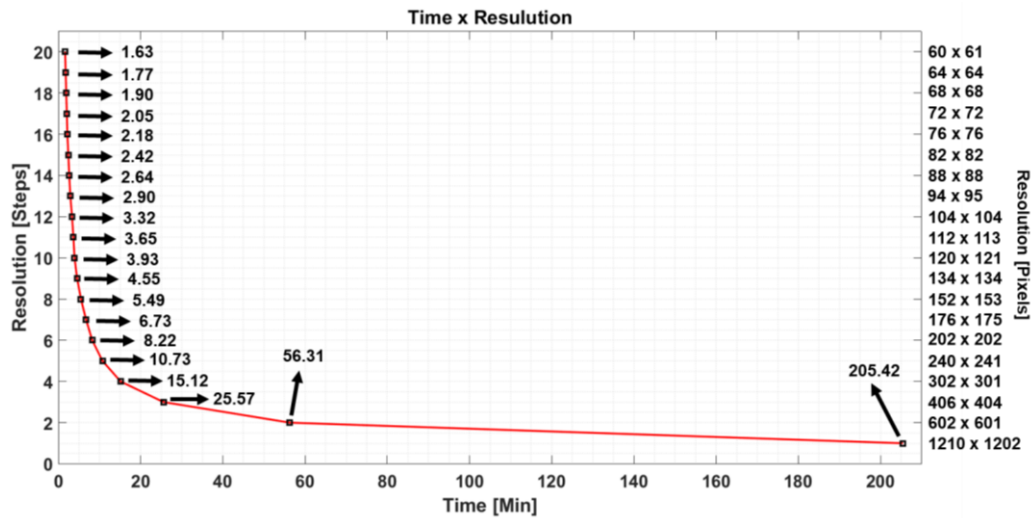


Figure 10. Graph depicting the time taken to complete one measurement cycle as a function of resolution, which is the number of steps the motors rotate at each measurement point. It is possible to observe a decay inversely proportional to the square of the resolution indicating how the variables of resolution and time to complete a measurement cycle are related. As the resolution in pixels increases, meaning that the number of steps the XY motors rotate at each measurement point decreases, the time to complete the measurement cycle also increases.

To increase the signal to noise ratio of the measurement, it is the average of N ($1 \leq N \leq 100$) measurements that is stored per pixel. This property is adjusted with the help of the ACCURACY slide on the GUI. It is important to note that a higher accuracy will result in a longer time for the instrument to complete a measurement matrix, following a linear trend, as can be seen in Figure 11.

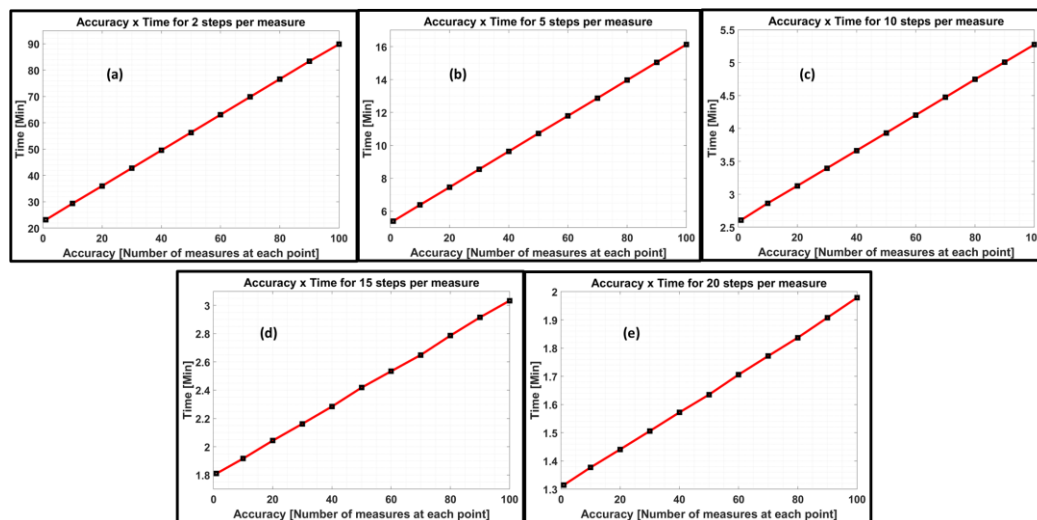


Figure 11. Graphs representing the time elapsed to finish a measurement cycle as a function of accuracy, that is, the number of measurements that the microcontroller performs at each point, for (a) 2-step resolution, (b) 5-step resolution, (c) 10-step resolution, (d) 15-step resolution, (e) 20-step resolution.

Once the accuracy and resolution settings are set, the instrument will position the receiving antenna at the starting point of the measurements, and the operator must then choose the type of characterization to be performed. Figure 9 depicts three buttons on the GUI: DISTANCE, ANGLE, and BOTH. The DISTANCE option is used when the operator wants to execute measurements by only varying the distance between the metasurface and the receiving antenna. The ANGLE button is

The subsequent step involves setting the angle parameters between the metasurface and the receiving antenna. The operator first specifies the initial angle by adjusting the value of the INITIAL ANGLE slider, within a range of -45° to 45° , with 0° being the point at which the metasurface is perpendicular to the receiving antenna. The operator then sets the final angle for the measurements by adjusting the FINAL ANGLE slider. It is important to note that the difference between the absolute value of the initial and final angles must always be greater than the value set in the ANGLE STEP slider. If the FINAL ANGLE and ANGLE STEP sliders are configured to values that are not permissible, the GUI will display an error message and block the SEND buttons for these two settings.

Figure 12 depicts the system operation. Functions performed by the microcontroller of the main board (Mega) are represented in green, functions performed by the secondary board (Uno) are represented in blue, and functions performed in the GUI (Raspberry Pi 4) where the operator performs the equipment configurations are represented in red. Figure 12(b) is the loop part (in green) that appears in Figure 12(a) within the 3 modes of equipment operation. It is separated to provide a clearer demonstration of how the instrument operates.



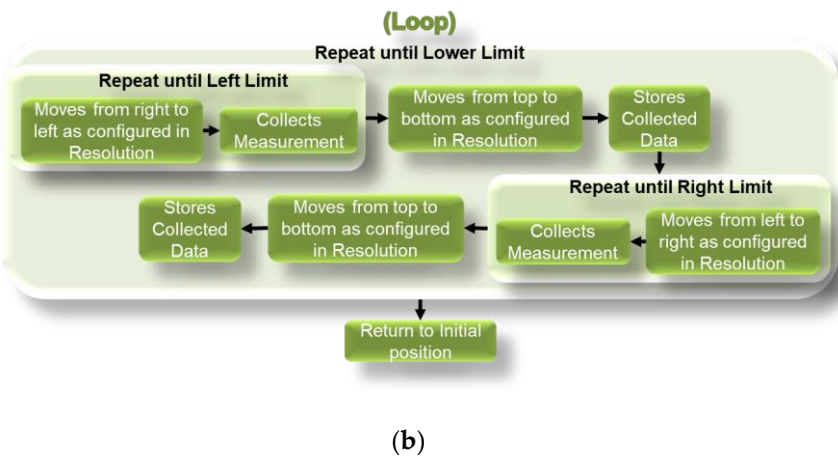


Figure 12. Schematic with step by step how the instrument works. (a) The entire schematic. (b) Loop part only.

6. Results and Discussion

In order to assess the practical utility of our equipment, the device was employed in the characterization of a 3D printed metalens, fabricated with the thermoplastic Polylactic acid (PLA). The PLA plastic microwave permittivity were extracted according to [22]. The results obtained from the instrument were then compared to those obtained from computer simulations.

The Metalens design used a hyperbolic phase profile with 20cm focal length, adjusted to operate at 30GHz [23]. It has a square area with sides measuring 15cm. The phase control is made with 3D printed prisms with varying side length, which act as a truncated waveguides [7,24]. The unit cell size is 6mm and the posts are 18mm tall. The phase profile was sampled using eight phase levels, which required the same amount of different structures in the design. More details can be found in [7]. Figure 13 illustrates the fabrication processes involved in the metalens manufacturing.

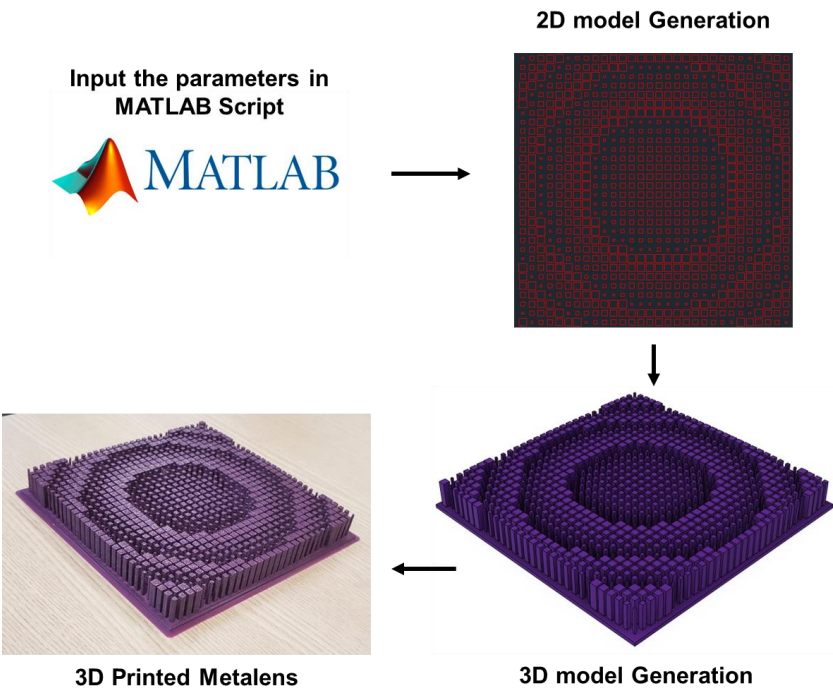


Figure 13. Step-by-step of metalens fabrication.

First, the transmitted fields of the metalens was simulated using the scalar Angular spectrum formalism [25] and using the local post approximation [26]. Figure 14 shows the normalized inten-

sity distribution on at increasing distances from the metalens by 2cm of increment starting at 12cm (Figure 14(a)) and finishing at 28cm (Figure 14(i)). The intensity normalization in these reconstructions was performed considering the maximum and the minimum intensity of each distance matrix separately.

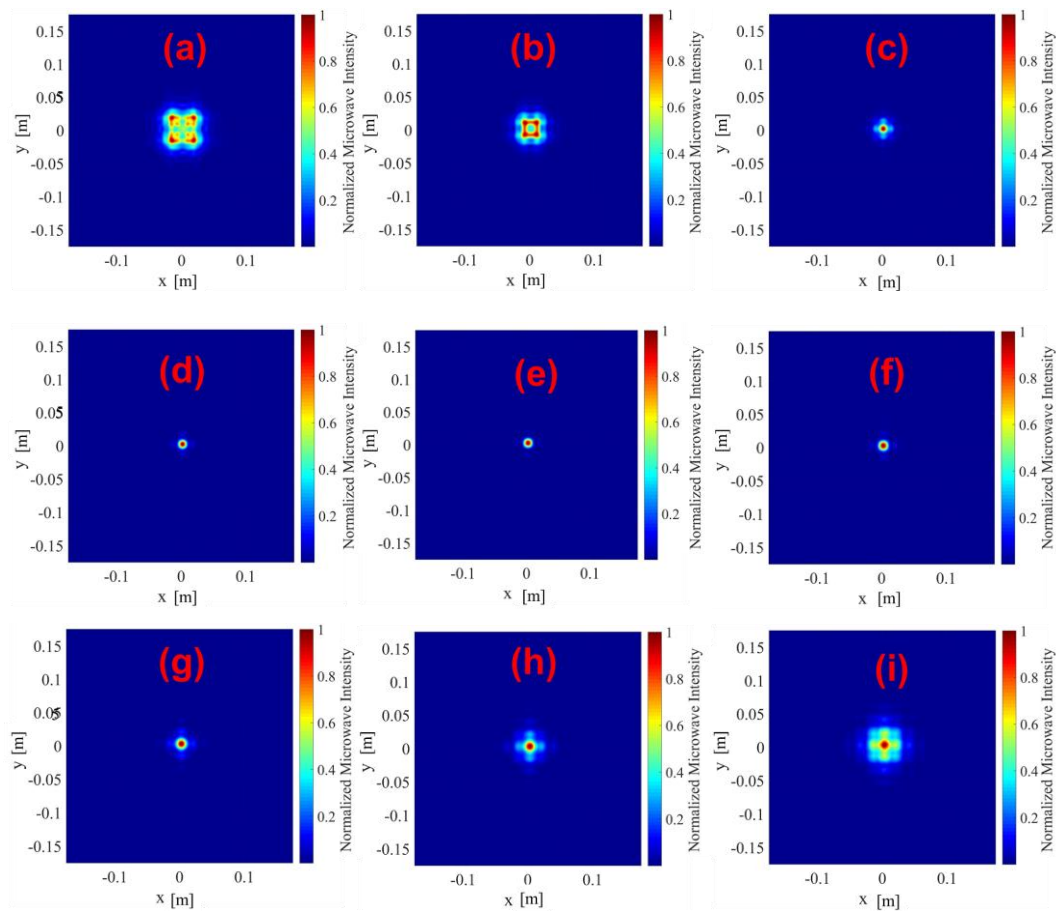


Figure 14. Simulated and normalized intensity profiles on planes placed at different distances after the metalens obtained with simulations. (a)-(i) show the results on planes that are 1cm, 14cm, ..., 26cm and 28cm, respectively. The operating frequency is 30GHz.

Figure 15 shows the normalized measured intensity distribution transmitted by the metalens, where (a)-(i) shows the intensity field at 12cm to 28cm, respectively, with steps of 2cm. The intensity normalization was performed similarly the metalens simulation to maintain consistency in the comparison. These reconstructions provide a comprehensive view of the intensity distribution transmitted by the metalens at various distances from the receiving antenna and they match quite well with the simulated intensity profiles shown on Figure 14. The instrument GUI was configured with the following parameters to obtain the fields depicted in Figure 15: a resolution of three steps per measurement and fifty measurements (accuracy) at each point. These settings resulted in the production of images with a size of 400 by 400 pixels. The good agreement between the simulation and the measurements highlights the high accuracy of the instrument and the quality of the fabricated metalens. This validation is crucial to ensure the accuracy and reliability of the results obtained from the use of the instrument for other future purposes.

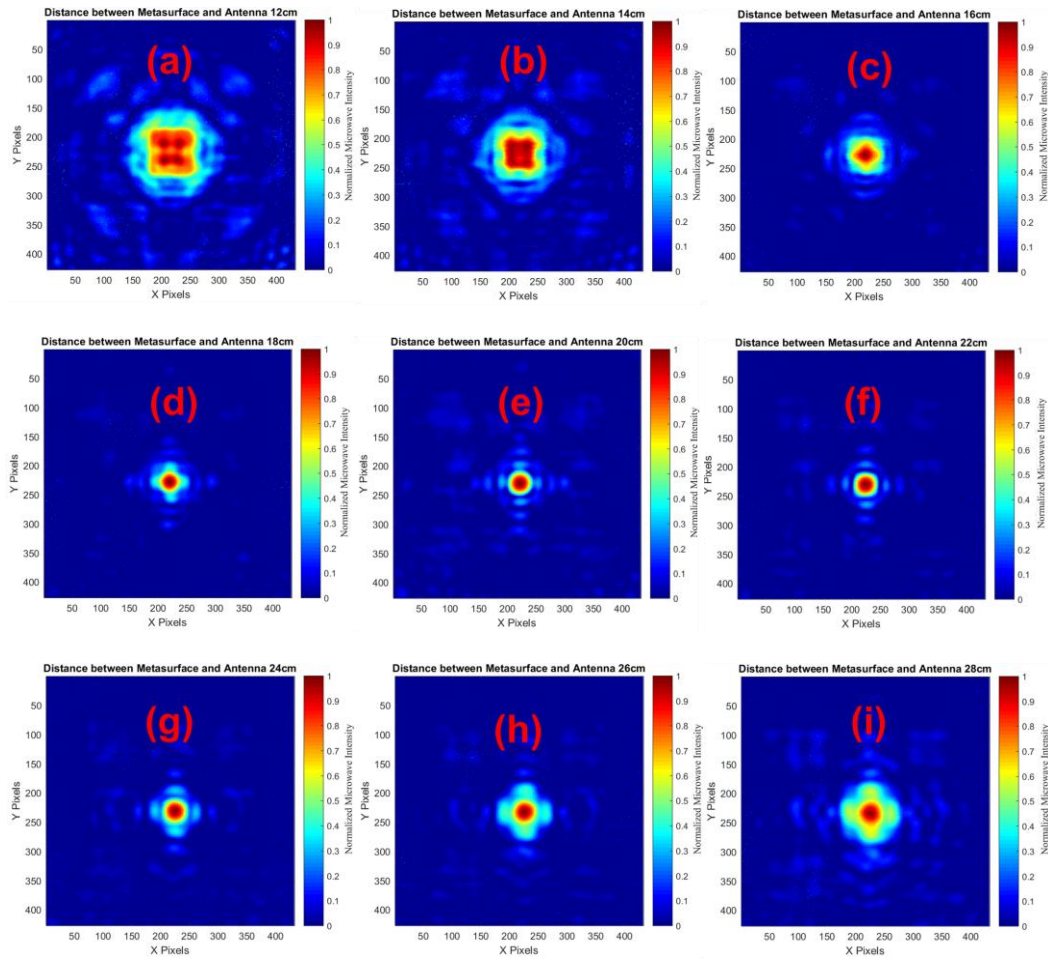


Figure 15. Measured and normalized intensity profiles on planes placed at different distances after the metalens. (a)-(i) show the results on planes that are 12cm, 14cm, ..., 26cm and 28cm, respectively. The operating frequency is 30GHz.

Upon analysis of Figures 14 and 15, a definitive determination of the actual focal length, previously stated as 20cm, cannot be made. Thus, to establish the correspondence of the metalens behavior with the intended design, Figure 16 exhibits the intensity fields, encompassing all the extracted measurements, where (a)-(i) shows the intensity field at a distance of 12cm to 28cm, respectively, with steps of 2cm, similar to Figures 14 and 15. Figure 16(e) exhibits conspicuously more intense measurements than the other figures, reaching a maximum intensity of $6.25V^2$, attesting to the consistency of the focal length with the originally intended specifications.

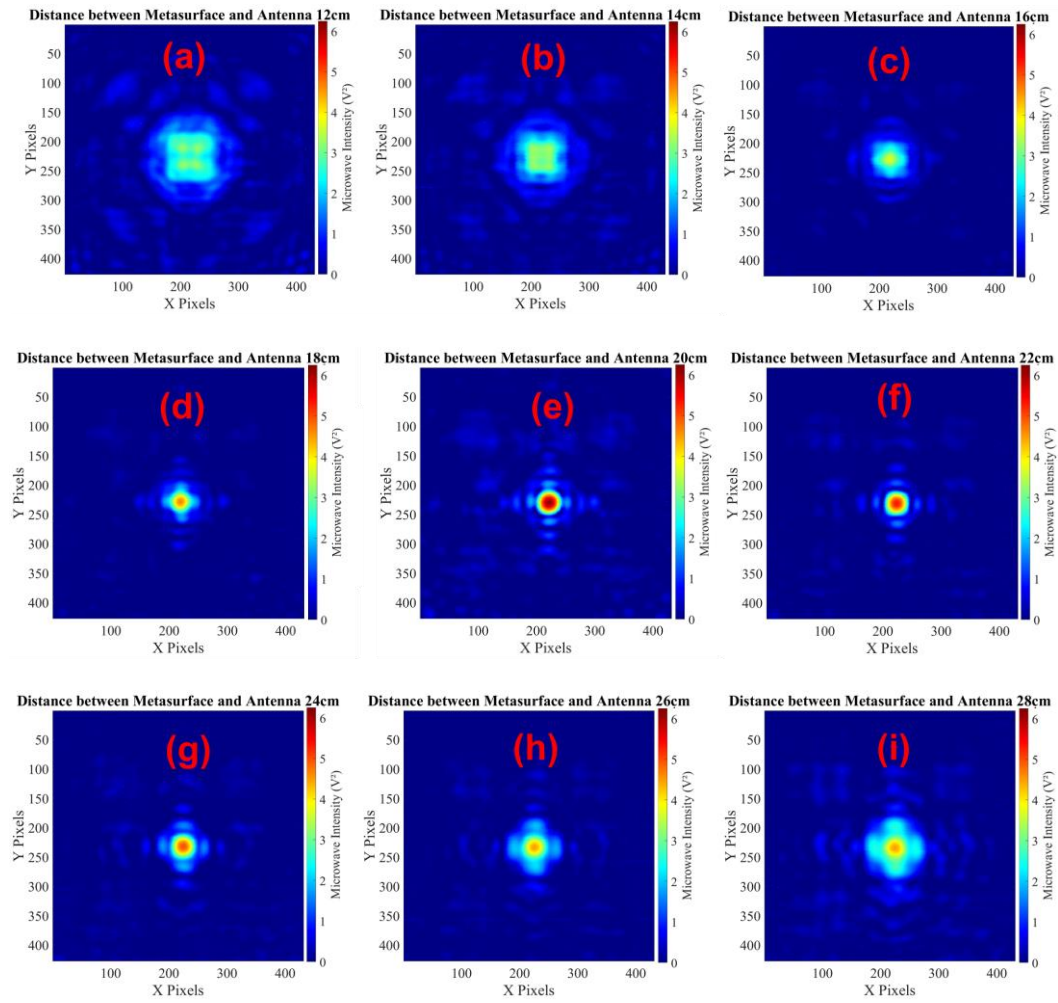


Figure 16. Measured intensity profiles, considering all the extracted intensity measurements on planes, placed at different distances after the metalens. (a)-(i) show the results on planes that are 12 cm, 14cm, ..., 26cm and 28cm, respectively. The operating frequency is 30GHz.

The instrument's effectiveness has been demonstrated through the comparison of results obtained by measuring metalens intensity profiles with those obtained by computational simulation. This validation enables to further explore the primary functionality of our developed instrument, which is the 3D reconstruction of the transmitted metalens intensity profiles surface. Figure 17 illustrates these measured reconstructions, showcasing the ability of the instrument to accurately measure the three-dimensional intensity profiles produced by the metalens. It was necessary to crop 1/4 of the 3D reconstruction in Figure 17 to observe the innermost layers of the fields produced by the metalens. Note that the signal intensity increases as it approaches the focal length of the lens, reaching its maximum at 20cm, which is designed focal distance.

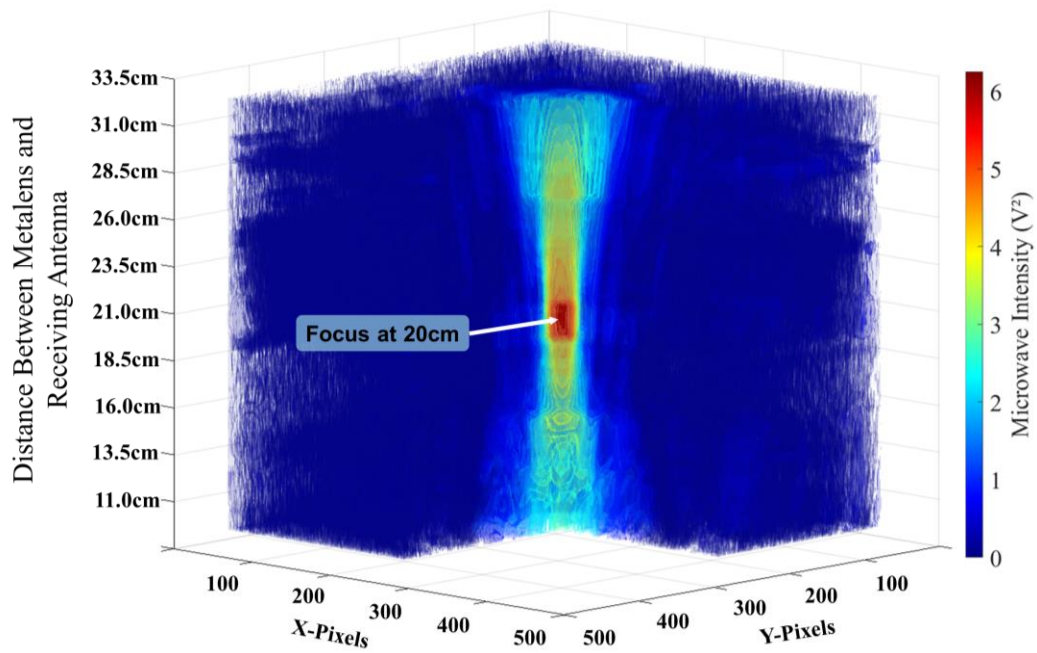


Figure 17. 3D reconstruction of the measured intensity fields produced by the metalens.

We used the previous measurements to characterize the metalens quantitatively with the 3dB depth-of-focus (DOF) and the full width at half maximum (FWHM), located 20cm away from receiving antenna. Figure 18 presents the 3D reconstructions of the measured intensity surfaces until the 3dB decay. Therefore, we measured a 11cm 3dB DOF and a 2.17cm FWHM as can be shown in Figures 18 (a) and (b), respectively.

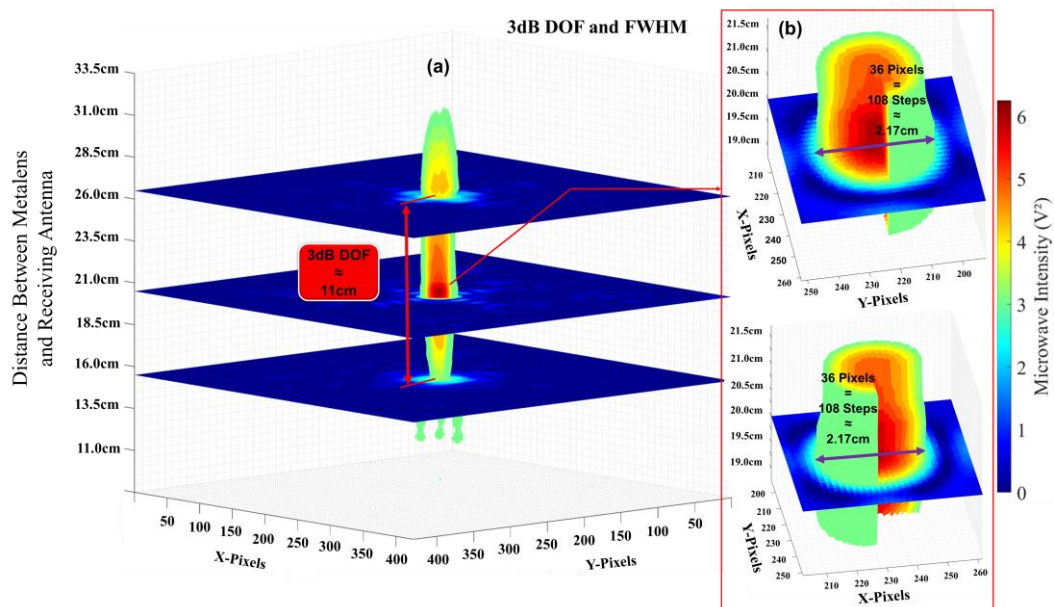


Figure 18. 3D reconstructions of the measured intensity surfaces until the 3dB decay. (a) 3dB DOF limits and (b) Zoom at focal plane showing the focal FWHM.

To conclude, another parameter characterized and extracted from our manufactured metalens was the gain. A measurement cycle without the metalens positioned between the transmitting and receiving antennas was conducted to measure the signal intensity without modulation from the metalens. The result can be seen in Figure 19(a).

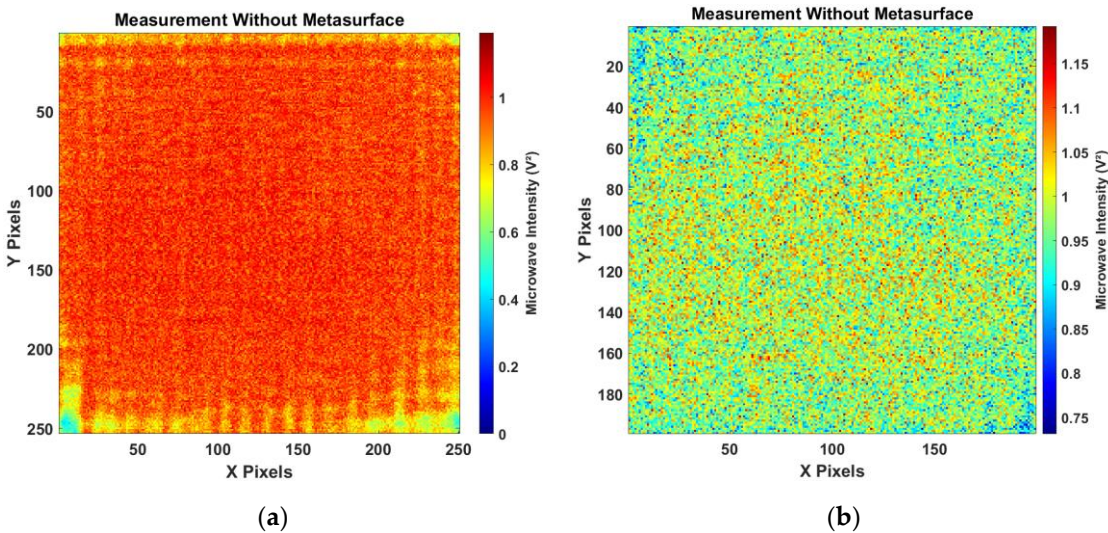


Figure 19. measurement cycle without the metalens positioned between the transmitting and receiving antennas: **(a)** The complete matrix extracted from the measurements; **(b)** central part of the matrix, excluding 50 pixels on each side.

It is noticeable that there is a pronounced signal oscillation at the edges of the matrix, caused by the presence of metal bearings, shafts, sensors, and motors at the edges. Therefore, it is appropriate to analyze the central part of the matrix shown in Figure 19(b), discarding the edges. To extract the gain of the metalens, it was necessary to compare the intensity measured by the instrument at the focal distance with the intensity measured when there isn't metalens between the antennas. Figure 16(e) shows the matrix extracted at the focal distance, reaching a maximum intensity of 6.25V². The average intensity collected in the scan without the metalens was 0.98V², and comparing the two results, a ratio of 6.25/0.98 yields 6.38 times. Applying the logarithm: 10log(6.38) results in a gain of 8.05dB.

7. Conclusions

In summary, this paper introduced a highly versatile and low-cost instrument for the precise characterization of microwave metasurfaces, with a specific focus on the Ka Band. The instrument is capable of accurately fully characterize a metalens, allowing for a reliable characterization of the point spread function in terms of usual parameters such as the DOF and FWHM and gain, which were quantified as 11cm, 2.17cm and 8.05dB, respectively, for the measured metalens. Moreover, the instrument can generate data for an unprecedented 3D reconstruction of the intensity distribution of the metalens, providing a more comprehensive understanding of its properties. Taken together, these findings strongly suggest that the instrument represents a highly valuable tool for the precise and comprehensive characterization of metasurfaces across a broad range of potential applications. Table 1 lists the components of the instrument and the cost for each component. Moreover, at the end of the Table 1, the total cost of the device.

Table 1. Cost of each component of our instrument and, in the end, total cost,.

Component	Quantity	Cost
Stepper Motor	6 units	81.22 USD
Micro Switch	7 units	3.87 USD
Raspberry Pi 4 8Gb RAM	1 unit	305.15 USD
Kit Keyboard and Mouse	1 unit	22.88 USD
Display 10 in. and Controller Board	1 unit	54.47 USD
Arduino Mega	1 unit	43,56 USD
Arduino Uno	1 unit	24,84 USD
DRV8825 Driver	6 units	25.65 USD

Main Board PCB	1 unit	1.90 USD
Secondary Board PCB	1 unit	0.40 USD
Angle Board PCB	1 unit	0.40 USD
Power Supply 12V 10A	1 unit	7.63 USD
HC-05 Bluetooth Module	2 units	10.68 USD
Cooler Fan	5 units	13.92 USD
HW-203 SD Card Module	1 unit	4.18 USD
DC2158A Board	1 unit	543.62 USD
KMM36 RF Cable	1 unit	157.50 USD
Antenna	1 unit	3.82 USD
Flexible Coupler 5x6mm	1 unit	3.43 USD
GT2 Timing Pulley	4 units	11.07 USD
GT2 Bearing	4 units	15.05 USD
Timing Belt GT2	3.17 m	6.02 USD
Threaded Bar	0.51 m	2.33 USD
Acrylic 12mm	0.487 m ²	92.08 USD
Acrylic 6mm	0.172 m ²	16.28 USD
Acrylic 3mm	0.006 m ²	0.30 USD
ABS	5.75 Kg	98.68 USD
TOTAL		1550.93 USD

Author Contributions: Conceptualization, R.H., A.M. and V.P.; methodology, R.H. A.M. and V.P.; software, R.H.; validation, R.H.; formal analysis, R.H.; investigation, R.H.; resources, R.H. and A.M.; data curation, R.H.; writing—original draft preparation, R.H.; writing—review and editing, R.H. and J.P.C.; visualization, R.H., B.H.V.B. and J.P.C.; supervision, J.P.C.; project administration, J.P.C.; funding acquisition, B.H.V.B. and J.P.C. All authors have read and agreed to the published version of the manuscript.

Funding: This research work was supported by through the National Council for Scientific and Technological Development (CNPq), which is a foundation linked to the Ministry of Science and Technology (MCT), to support Brazilian research. The CNPq process number was 303562/2017-0. The author was supported by a Coordination for the Improvement of Higher Education Personnel (CAPES) scholarship with process number: 88887.4829072020-00. scholarship with process number: 88887.4829072020-00.

Institutional Review Board Statement: Not applicable.

Informed Consent Statement: Not applicable.

Data Availability Statement: Not applicable.

Acknowledgments: We would like to express our sincere gratitude to the Electrical and Computer Engineering Department (SEL) at the São Carlos School of Engineering (EESC) from University of São Paulo (USP). We would also like to acknowledge the research funding agencies CNPq and CAPES for their support in this work.

Conflicts of Interest: The authors declare no conflict of interest. The funders had no role in the design of the study; in the collection, analyses, or interpretation of data; in the writing of the manuscript; or in the decision to publish the results.

References

1. Shrestha, S.; Baba, A.A.; Abbas, S.M.; Asadnia, M.; Hashmi, R.M. A Horn Antenna Covered with a 3D-Printed Metasurface for Gain Enhancement. *Electronics (Switzerland)* **2021**, *10*, 1–12, doi:10.3390/electronics10020119.

2. Shrestha, S.; Zahra, H.; Abbasi, M.A.B.; Asadnia, M.; Abbas, S.M. Increasing the Directivity of Resonant Cavity Antennas with Nearfield Transformation Meta-Structure Realized with Stereolithography. *Electronics (Switzerland)* **2021**, *10*, 1–12, doi:10.3390/electronics10030333.

3. Liu, C.; Hu, C.; Wei, D.; Chen, M.; Shi, J.; Wang, H.; Xie, C.; Zhang, X. Generating Convergent Laguerre-Gaussian Beams Based on an Arrayed Convex Spiral Phaser Fabricated by 3D Printing. *Micromachines (Basel)* **2020**, *11*, doi:10.3390/MI11080771.
4. Gan, Y.; Meng, H.; Chen, Y.; Zhang, X.; Dou, W. Generation of Bessel Beams with 3D-Printed Lens. *International Journal of RF and Microwave Computer-Aided Engineering* **2020**, *30*, doi:10.1002/mmce.22029.
5. Viskadourakis, Z.; Tamiolakis, E.; Tsilipakos, O.; Tasolamprou, A.C.; Economou, E.N.; Kenanakis, G. 3d-Printed Metasurface Units for Potential Energy Harvesting Applications at the 2.4 GHz Frequency Band. *Crystals (Basel)* **2021**, *11*, doi:10.3390/cryst11091089.
6. Liu, Y.Q.; Sun, J.; Qi, K.; Che, Y.; Li, L.; Yin, H. High-Numerical-Aperture(NA) Microwave Metasurface Lens(Metalens) and Its Applications in High-Gain Antenna. In Proceedings of the 2021 19th International Conference on Optical Communications and Networks, ICOCN 2021; Institute of Electrical and Electronics Engineers Inc., 2021.
7. Pepino, V.M.; Da Mota, A.F.; Martins, A.; Borges, B.H. V. 3-D-Printed Dielectric Metasurfaces for Antenna Gain Improvement in the Ka-Band. *IEEE Antennas Wirel Propag Lett* **2018**, *17*, 2133–2136, doi:10.1109/LAWP.2018.2860521.
8. Alex-Amor, A.; Palomares-Caballero, Á.; Molero, C. 3-D Metamaterials: Trends on Applied Designs, Computational Methods and Fabrication Techniques. *Electronics (Switzerland)* **2022**, *11*.
9. Bukhari, S.S.; Vardaxoglou, J.; Whittow, W. A Metasurfaces Review: Definitions and Applications. *Applied Sciences (Switzerland)* **2019**, *9*.
10. Kang, M.; Ra'Di, Y.; Farfan, D.; Alù, A. Efficient Focusing with Large Numerical Aperture Using a Hybrid Metalens. *Phys Rev Appl* **2020**, *13*, doi:10.1103/PhysRevApplied.13.044016.
11. Jilani, S.F.; Falade, O.P.; Wildsmith, T.; Reip, P.; Alomainy, A. A 60-GHz Ultra-Thin and Flexible Metasurface for Frequency-Selective Wireless Applications. *Applied Sciences (Switzerland)* **2019**, *9*, doi:10.3390/app9050945.
12. Martínez-Llinàs, J.; Henry, C.; Andrén, D.; Verre, R.; Käll, M.; Tassin, P. A Gaussian Reflective Metasurface for Advanced Wavefront Manipulation. *Opt Express* **2019**, *27*, 21069, doi:10.1364/oe.27.021069.
13. Wang, X.; Wu, J.; Wang, R.; Li, L.; Jiang, Y. Reconstructing Polarization Multiplexing Terahertz Holographic Images with Transmissive Metasurface. *Applied Sciences (Switzerland)* **2023**, *13*, doi:10.3390/app13042528.
14. Pung, A.J.; Goldflam, M.D.; Burckel, D.B.; Brener, I.; Sinclair, M.B.; Campione, S. Enhancing Absorption Bandwidth through Vertically Oriented Metamaterials. *Applied Sciences (Switzerland)* **2019**, *9*, doi:10.3390/app9112223.
15. Tishchenko, A.; Ali, A.; Botham, P.; Burton, F.; Khalily, M.; Tafazolli, R. Reflective Metasurface for 5G MmWave Coverage Enhancement. In Proceedings of the 2022 International Symposium on Antennas and Propagation, ISAP 2022; Institute of Electrical and Electronics Engineers Inc., 2022; pp. 507–508.
16. Chen, Z.N.; Li, T.; Li, S.; Xue, C.; Lou, Q.; Liu, W.E.I. Microwave Metalens Antennas for 5G Network. **2021**, doi:10.1002/j.1538.
17. Rahamim, E.; Rotshild, D.; Abramovich, A. Performance Enhancement of Reconfigurable Metamaterial Reflector Antenna by Decreasing the Absorption of the Reflected Beam. *Applied Sciences (Switzerland)* **2021**, *11*, doi:10.3390/app11198999.
18. Rohde & Schwarz R&S®ZVA Vector Network Analyzer Specifications; 2015.
19. Pasternack WR-34 Standard Gain Antenna PE9851-2F-20, 2013.
20. Kraus, J.D. The Helical Antenna. *Proceedings of the IRE* **1949**, *37*, 263–272, doi:10.1109/JRPROC.1949.231279.
21. Analog Devices Ultralow Offset Voltage Operational Amplifier; 2011.
22. Picha, T.; Papezova, S.; Picha, S. Evaluation of Relative Permittivity and Loss Factor of 3D Printing Materials for Use in RF Electronic Applications. *Processes* **2022**, *10*, doi:10.3390/pr10091881.
23. Yin, X.; Zhu, H.; Guo, H.; Deng, M.; Xu, T.; Gong, Z.; Li, X.; Hang, Z.H.; Wu, C.; Li, H.; et al. Hyperbolic Metamaterial Devices for Wavefront Manipulation. *Laser Photon Rev* **2018**, *13*, doi:10.1002/lpor.201800081.
24. Guo, B.; Jiang, L.; Hua, Y.; Zhan, N.; Jia, J.; Chu, K.; Lu, Y. Beam Manipulation Mechanisms of Dielectric Metasurfaces. *ACS Omega* **2019**, *4*, 7467–7473, doi:10.1021/acsomega.9b00641.
25. Novotny, L.; Hecht, B. *Principles of Nano-Optics*; Cambridge University Press, 2012; ISBN 9781107005464.

26. Martins, A.; Li, J.; da Mota, A.F.; Wang, Y.; Neto, L.G.; do Carmo, J.P.; Teixeira, F.L.; Martins, E.R.; Borges, B.-H. V. Highly Efficient Holograms Based on C-Si Metasurfaces in the Visible Range. *Opt Express* **2018**, *26*, 9573, doi:10.1364/oe.26.009573.